International Journal of Education and Science Research Review
E-ISSN 2348-6457
Sep-Oct- 2017, Volume-4, Issue-5
P-ISSN 2349-1817
www.ijesrr.org
Email- editor@ijesrr.org

MAGNESIUM NICKEL FERRITE NANOPARTICLES' STRUCTURAL MAGNETIC AND ELASTIC PROPERTIES AS A FUNCTION OF ANNEALING TEMPERATURE.

Lavkush Kumar

Associate Professor in Physics RH govt PG college

kashipur dist u s nagar uttarakhand.

Dr. B.Lal

Department of Physics

Swami Sharaddha Nand college (University of Delhi)

ABSTRACT

The proposed work illustrates the aqueous synthesis of sol-gel-produced MgNi ferrite nanoparticles. In a water-based synthesis, citric acid served as the fuel and the nitrates of magnesium, nickel, and iron as the precursors. The ferrites were annealed at temperatures of 900°C and 1100°C to extract the best qualities from them. The nanoparticles that were created were characterised using the X-ray diffraction technique (XRD), field emission scanning electron microscopy (FESEM), transmission electron microscope (TEM), vibrating sample magnetometer (VSM), FTIR spectroscopy, and Raman spectroscopy in order to learn about their structural, morphological, elastic, and magnetic properties. The inverse-spinel structure with crystallite sizes of 35–61 nm and 66–94 nm for ferrites annealed at 900°C and 1100°C, respectively, is confirmed by structural analyses and the results of XRD, FTIR, and Raman spectroscopic patterns. Through absorption bands that correspond to the vibration of the tetrahedral site-A and the octahedral site-B, respectively, the creation of the spinel ferrite structure is proven. Williamson-Hall plots were used to calculate crystallite size. To guarantee the crystal structure and related properties, the Rietveld refinement method was used. When the produced samples were subjected to a magnetic analysis using VSM, the results showed that the nanoparticles displayed superparamagnetic behaviour with high magnetic saturation (MS) and low coercivity (HC). When the same precursor is annealed at higher temperatures, such as 1100C, the assessment of elastic characteristics by absorption bands shows an improvement. The MgNi ferrite spinel nanoparticles SNPs were the first material to successfully use the uniform deformation model (UDM), uniform stress deformation model (USDM), and uniform energy deformation model (UEDM). Three deformations were used to estimate the elastic constants and compliances and study the elastic characteristics. A final investigation that compared the results of two sets of samples reveals that the stability factor increases when samples are annealed at higher temperatures.

KEYWORDS: ***Elastic Properties, Annealing Temperature***

INTRODUCTION

Due to their excellent biocompatibility, low toxicity, and magnetism, ferrites spinels, where A is a divalent transition metal (Ni, Zn, Fe, Cr, Mn, Co), have gained a lot of attention in recent years. For technological and medical applications such as magnetocaloric refrigerators, magnetic memory, solar water oxidation, electrochemical supercapacitor applications, biological applications, lithium-ion batteries, contrast enhancement in magnetic resonance imaging (MRI), and magnetic uid hyperthermia, these materials are currently regarded as some of the most successful magnetic nanoparticles (MNPs). Consequently, from both a theoretical and practical standpoint, it is crucial to understand the structural and magnetic characteristics of spinels. The distribution cation and/or structural characteristics of these properties can be changed by altering the synthesis techniques, annealing temperature, and/or doping the appropriate elements into the A-site or B-site. The face-centered cubic (fcc) structure of ferrite spinel is made up of a cubic close-packed oxygen lattice. A spinel ferrite's unit cell is made up of 32 oxygen ions, 8 divalent metal ions (M), and trivalent iron ions.

Two interstitial positions in the spinel structure are occupied by metal cations that have oxygen coordinated octahedra (B) and tetrahedra (A). The inversion degree (g), which is defined as the percentage of divalent ions in the octahedral sites, serves as a general measure of the cationic distribution between the two sites. The octahedral sites in a normal spinel configuration are occupied by Fe3+ ions, whereas the tetrahedral sites are occupied by M2+, producing the empirical formula (M2+) A [Fe3+] B O4. Nevertheless, in inverse spinels, half of the Fe3+ ions are found in the tetrahedral sites, while the other half are found in the octahedral sites. This results in the empirical formula (Fe3+) A [M2+Fe3+] B O4.

Spinels can also be mixed in the structure. Yet, two ferromagnetically ordered sub-lattices result from superexchange interactions between magnetic atoms situated in the same class of interstitial sites (JA-A and JB-B). Yet, the predominant antiferromagnetic interactions between the magnetic ions in the A and B sites (JA-B) result in the induction of a non-compensated antiferromagnetic order between the two sub-lattices (ferrimagnetism). The greater surface area of nanoparticles leads to surface relaxation, surface bond bending, surface effect, and subsequently spin canting, which alter the relative importance of each interaction. For nano ferrites, it is important to carefully evaluate the relationship between structures and physical characteristics.

In order to create nano-spinel ferrite with diverse sizes and shapes, numerous methods, such as forced hydrolysis in polyol, ball milling, coprecipitation, sol-gel auto-combustion, and hydrothermal/solvothermal approach, etc., 3,11–14, have been extensively researched. Ball milling is a good means to create highly crystalline nanostructures, however it almost invariably results in agglomeration due to the high reaction temperature and extended reaction time.

In contrast, the sol-gel approach is favoured because it offers superior control over particle formation shape and size at low temperatures and in a short period of time while maintaining a high level of purity. The advantages of this technology include its low cost and high-quality output. 15 A member of the spinel ferrites class, Ni-Zn ferrite is well known for its use in magnetic, magnetooptical, and magnetodielectric devices. Spinel Ni-Zn ferrites are a typical ferrimagnetic material with mixed spinel structure (Fei 3+M1i 2+)[Mi 2+- Fe2i 3+] under normal circumstances. O4, 16, and 17 belong to the Fd3m space group, and where I is the inversion degree, () and [] stand for the tetrahedral and octahedral locations, respectively. There are two extreme examples where the cation configuration can change.

One of these is the common spinel I 14 0), which has all the trivalent elements in octahedral B sites and all the divalent elements in tetrahedral A sites. The other is the inverse spinel I 14 1), in which all of the trivalent

elements are equally distributed between tetrahedral A sites and octahedral B sites while all of the divalent elements occupy octahedral B sites. Moreover, partially inverse spinels (i.e., spinels with a cation distribution between normal and inverse; 0 I 1) are relatively common. 18 The high surface area, chemical stability, high saturation magnetization, high Curie temperature, low coercivity (so magnetic), high permeability, high dielectric constant, low losses, semiconductor dielectric transition, and wide application in the high frequency region of electronics devices are additional characteristics of Ni-Zn ferrites.

MAGNETIC NANOPARTICLES

Magnetic nanoparticles are nanoparticles that can be controlled, tracked, and targeted using an external magnetic field (MNPs). The magnetic material of these MNPs, which includes elements like iron, cobalt, and nickel, is one component, while the chemical functionality is the other. These nanoparticles range in size from one to one hundred nanometers[15, 16]. With magnetic nanoparticles (MNPs), the methods used in their manufacturing as well as the components that make them up determine both their physical and chemical properties. They are divided into four categories based on these two criteria: first, oxides or (Ferrites) ii) Metals iii) Metals iv) Metals with Shell iii) Oxides (Ferrites) with Shell

FERRITES

The oxides of magnetic elements like Fe, Ni, Mn, etc. are known as ferrites. First, it is well known that iron (ferrum) and later other materials like nickel, cobalt, etc. display magnetic at ambient temperature. These substances belong to the class of magnetic materials known as ferrites and are often magnetic ceramics. As soon as ferrite nanoparticles reach a particle size of less than 128 nanometers during the production process, they become superparamagnetic, which also prevents them from self-aggregating. The magnetic moments of the magnetic material abruptly increase when individual superparamagnetic nanoparticles carefully arrange themselves into beads in the shape of superparamagnetic clusters. Such behaviour in ferrite particles can only be induced by an external magnetic field. Their residual magnetism instantly decreases to zero when the external magnetic field is turned off, and they begin to act as nonmagnetic oxide nanoparticles.

.OBJECTIVE OF STUDY

1. Study On Magnesium Nickel Ferrite Nanoparticles' Structural Magnetic
2. Study On crystal structure that these materials adopted throughout their manufacture largely determines the attributes of ferrites.

RESEARCH METHOLOGY

Synthesis in the experimental section Without additional purification, all of the chemical reactants used in this work were acquired from Sigma-Aldrich. Using the sol-gel process, Ni0.6- Zn0.4Fe1.5Al0.5O4 nanoparticles were successfully created. In other places, the procedure was thoroughly explained. 23 In a typical preparation, distilled water was used to dissolve analytical purity grade Fe(NO3)3$9H2O and NiCl2$6H2O. Nitric acid was used to dissolve the pure (99.99%) oxide powders ZnO and Al2O3. The acquired solution was combined with the original. We combined this solution with citric acid (C6H8O7) in a mixture with metal cations (Ni + Fe + Zn + Al) at a molar ratio of 1:1.5, which was achieved by adding ethylene glycol (C2H6O2). To eliminate the extra water and create a gel, the resultant solutions were heated to 80 C while being stirred magnetically. The

powder as prepared was annealed at 500 C for 6 hours in an electrical muffle furnace before being progressively cooled to room temperature in order to break down the organic content.

The finished powder was divided into a total of four sets and then pelletized and annealed at temperatures of 600, 800, 900, and 1050 C for six hours and 1200 C for twenty-four hours, respectively. Fig. 1 depicts the chemical reaction of the prepared sample. Measurements and characteristics

By using X-ray diffraction at room temperature, the structural characterisation was completed. Powder X-ray diffraction (XRD) on a Bruker D8 diffractometer with Cu Ka radiation (l 14 1.5406 A) and a step size of 0.015 width from 15 to 80 was used to describe the ferrite nanoparticles. Using Merlin scanning electron microscopy (SEM) with an energy-dispersive X-ray spectrometer, morphological characterisation was performed (EDXS). By using ImageJ software to process SEM images, the particle size was determined.

DATA ANALYSICS

The Setaram Instrument was used to do differential thermal analysis (DTA) and thermogravimetric analysis (TGA). In an argon atmosphere with a nitrogen flow of 40 ml per minute, the sample was heated to 1000 C at a rate of 10 C per minute. A SENTERRA spectrometer from the Bruker Company was used to capture the Raman spectra, which were excited by a 532 nm laser at room temperature. ambiant temperature Thermo Scientific Nicolet 6700 FTIR Spectrometer was used to obtain Fourier transform infrared (FTIR) spectra using the diffuse repentance infrared Fourier transform spectroscopy (DRIFTS) method in the 400–4000 cm1 range. Spectra of absorption were

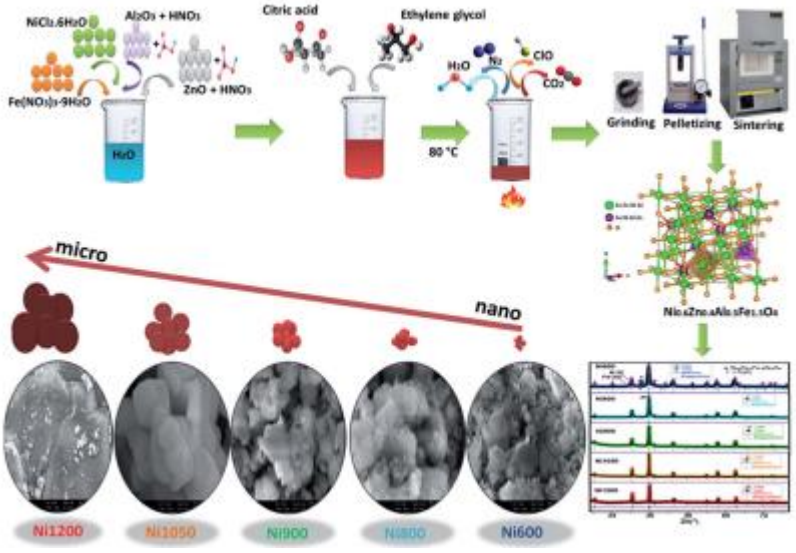

Fig. 1 Chemical reaction of Ni0.6Zn0.4Al0.5Fe1.5O4 synthesized by sol–gel method

recorded for the UV/visible/IR range on a UV-3600 Spectrophotometer (SHIMADZU, Japan). The NZFAO pellets were subjected to magnetostriction experiments utilising the short angle rotation magnetization technique. A SQUID magnetometer was used to record the magnetic isotherms M(H) at ambient temperature with a magnetic field of up to 4 T. Using a differential sample magnetometer called MANICS, measurements of the intrinsic magnetic temperature (TC) were made in a field up to 1 kOe. Also, the Bruker ESP-300E spectrometer was used to conduct the electron spin resonance (ESR) experiments. It operates in the X band at

9.3 GHz with a 2 GHz field modulation. Thermal evaporation is used to deposit a thin layer of silver on both sides of the pellet through a circular mask with an 8 mm diameter. It is possible to investigate the electrical properties of the synthetic material because a planar capacitor configuration has been created. Measurements are made using a vacuum-sealed Agilent 4294A analyzer with a 20 Mv signal amplitude.

Figure 2 displays the TGA and DTA curves of the as-prepared sample, which were performed up to a temperature of 1000 C at a heating rate of 10 C min1 in argon gas to observe various changes in the form of endothermic and exothermic peaks that demonstrate the phase transition during the heat treatment. Thermal analysis is used to understand the decomposition behaviour of the Ni-Zn ferrite precursors and the formation of metal oxides. Furthermore, the aggregate of the two portions results in a 24% overall weight loss. The dehydration of remaining water is attributed to the overall weight loss of 2% in the temperature range below 200 C. The second 22% weight loss on the TGA curve between 200 and 630 C may be the result of an autocatalytic oxidation-reduction reaction involving citrate acid and nitrate.

The sample becomes stable in terms of weight at temperatures over 630 C, and the weight loss at or around this temperature may be related to the occurrence of the metal oxide phase of ferrite, Ni0.6Zn0.4Al0.5Fe1.5O4. TGA and DTA data indicate that the organic components were destroyed above 630 C. Hence, the sample underwent further annealing at a temperature of 600 C. Building analysis Using the FULLPROF programme, Fig. 3a shows the Rietveld-reined X-ray powder diffraction (XRD) patterns for Ni0.6Zn0.4Fe1.5Al0.5O4 samples that were annealed at 600, 800, 900, 1050, and 1200 C.

The atomic plane reactions are recognised, and they support the production of the single phase cubic spinel structure with the Fd3m space group. With the sample (Ni600) that was annealed at 600 C, we observe the formation of some peaks due to the rhombohedral symmetry R3c as a second phase (Fe2O3) denoted by (*), which vanished at higher annealing temperatures. Many writers have noted the hematite phase up to the calcination temperature of 900 C. 26 The absence of other structures' diffraction peaks in the other samples suggested that the crystalline was of a high degree of purity.

Table S1 (ESI) contains a list of the Rietveld renement parameters. A low goodness of (c2) value that we observed indicates that the remaining samples are useful and the collected samples are of high quality. According to Fig. 3b, the breadth at half maximum of the (311) peak diminishes as the annealing temperature rises. The fact that diffraction peaks narrow and sharpen with rising temperature indicates that the average size of the crystallites rises correspondingly. Figure 3c depicts the Ni, Zn, Al, Fe, and O atoms' various Wyckoff positions as well as the crystal structure of Ni0.6Zn0.4Fe1.5Al0.5O4. From the study of X-ray data, Ni-Zn nanoparticles' lattice constant (apex) was calculated using the relation:12

$$a_{exp} = \frac{\lambda\sqrt{h^2 + k^2 + l^2}}{2 \sin \theta}.$$

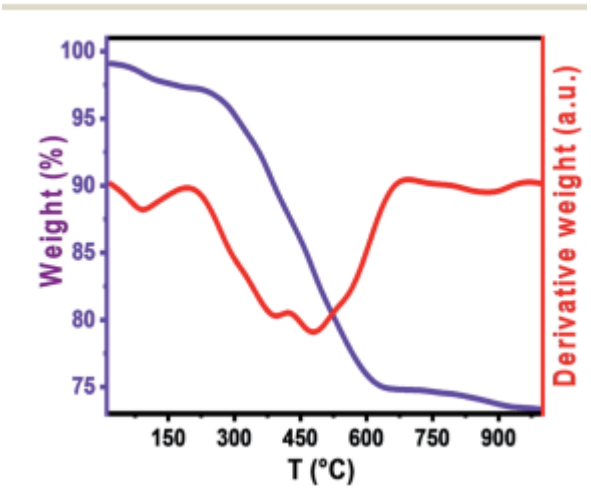

Fig. 2 TGA and DTA curves corresponding to solid sample obtained from NZAFO gel.

where h, k, and l are Muller indices, q is the diffraction angle, and l is the X-ray wavelength. The following equation has been used to determine the cubic system's unit cell volume: V ¼ aexp3 . In Fig. 3d, the volume of the ferrite compounds and all of the measured lattice characteristics are plotted versus the annealing temperature. A decrease in particle surface stress and the higher crystal structure of larger particles may both contribute to a drop in the lattice parameter with increasing annealing temperature. A reduction in particle size is also seen in many metal oxides' lattice parameters, which may be caused by cation/anion vacancies, the nite size effect, lattice stress, etc. For Ni-Zn ferrite nanoparticles, a comparable change of the lattice parameter has already been described. 11,21 Plotting the calculated "aexp" values of each diffraction peak vs the Nelson-Riley (N-R) function for each reaction of the examined Ni-Zn-Al ferrites also yields the true values of the lattice parameter "a0" using the extrapolation function F(q): 12

$$F(\theta) = \frac{1}{2}\left[\frac{\cos^2\theta}{\sin\theta} + \frac{\cos^2\theta}{\theta}\right]$$

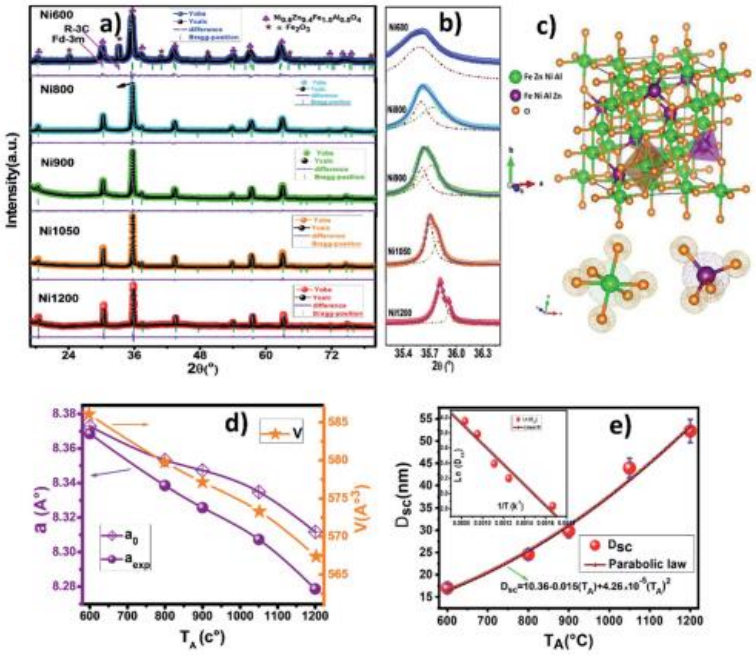

Figure 3 (a) shows the Ni0.6Zn0.4Al0.5Fe1.5O4 Rietveld refined X-ray diffraction patterns after being annealed at 600, 800, 900, 1050, and 1200 C. (b) Zoomed views in the interval of 2q between 35.3 and 36.3. ().

The sample's unit cell in (c) displays the tetrahedral (A) and octahedral (B) sites. (d) Ferrites compound lattice characteristics and volume against annealing temperature. (e) Dsc vs annealing temperature TA, where the fitted values are displayed and the solid line depicts the fit to the parabolic law.

In Fig. S1 (ESI), the values of the lattice constant "aexp" are shown as functions of F(q) for all samples. The genuine values of the lattice parameter are found to be marginally higher than the experimental values, as can be shown in Fig. 3d. It is also obvious that when particle size rose, "a0," "aexp," and volume all reduced.

In Table S1, all annealed samples' lattice parameters (a0, aexp, and aR determined from Rietveld rennement), density, porosity, crystallite size, and surface area are listed. The characteristics of polycrystalline ferrites are greatly affected by density. When the annealing temperature rises, the X-ray density (rX-ray), which ranges from 5.04 g cm3 for Ni600 to 5.15 g cm3 for Ni1200, rises as well. As a result, it has been discovered that the densification process is influenced by the annealing temperature. To put it another way, a force created by thermal energy causes grains to grow over pores during the sintering process, which lowers the volume of the pores and their grain borders.

The values of bulk density (rth) and porosity (P) both drop as particle size increases, indicating that the disorder of the spinel ferrite system is increased by annealing temperature. Sol-gel synthesis is well recognised for producing materials with a large surface area (S). Table S1 shows that the specific surface area ranged from 69.8 to 22.2. (m2 g1). As a result, ferrite with a large surface area is required for applications such as sensors and supercapacitors. 12 The conventional Scherer formula was used to determine the crystallite size from the line broadening of the peak with the highest intensity (311): 12,21

$$\beta \cos \theta = \frac{K\lambda}{D_{sc}}$$

where Dsc is the size of the crystal, K is the shape factor, l is the wavelength of the Cu Ka radiation (1.5406 A), q is the diffraction Bragg angle of the peak with the highest intensity (311) and b is the peak's half width in radians. It is evident from Fig. 3e that when the annealing temperature rises from 600 C to 1200 C, the crystallite size increases. Particularly when the sample is annealed over 900 C, the crystallite size significantly rises.

It is possible to credit the expansion of the crystallites to solid-state diffusion-driven coalescence, which is consistent with the rise in density. Figure 3f plots the matching crystallite size Dsc against the annealing temperatures. Plotting the calculated Dsc values against the annealing temperature TA reveals an increase with increasing particle size. The experimental data are represented by the red solid curve by a theoretical curve created using the parabolic law. The inset of Fig. 2f contains a list of the results' parameters. The inset of Fig. 3f depicts the logarithmic fluctuation in crystallite size for NZAFO NPs with annealing temperature in accordance with Coble's theory27. The modified Arrhenius equation can also be used to determine the activation energy of grain growth:

$$\ln(D) = \left(-\frac{E}{RT}\right) + \ln C$$

where T is the absolute temperature, R is the ideal gas constant, C is the particular reaction rate constant, and E is the activation energy. Hajalilou et al.28 observed that the crystallite growth activation energy of nickel ferrite produced by high-energy ball milling with Fe2O3 and NiO was 64.4 kJ mol1. This value is more than the current value of 11.3 kJ mol1, by comparison. This indicates that less energy was needed to break through the kinetic barrier during the formation of the Ni-Zn-Al ferrite crystallite produced by the sol-gel process. As a result, it contributes to the reason why phase Ni-Zn-Al spinel ferrite can be produced at lower temperatures. The Williamson-Hall method was used to compute the lattice strain (3). (gure not shown here). Table S1 clearly shows that strain continuously decreases as crystallite size increases. This is clear from the fact that as crystallite size grows, the ratio of atoms at the surface to those inside the volume drops, reducing the number of broken bonds for surface atoms and thus reducing strain.

The type of cation, its valence state, and its distribution on the spinel structure's tetrahedral A and octahedral B sites all affect the physical characteristics of ferrites. Consequently, comprehension of the complex link between structural and physical property is dependent on knowledge of the cation distribution. Using the use of measurements from the Mossbauer, XPS, X-ray diffraction, and Raman techniques, the distribution of cations in the various spinel ferrite systems has been determined. 29–31 According to Bestha et al.32, cations on the tetrahedral (A-) and octahedral (B-) site affect the intensities of the (220), (422), and (400) planes. In our investigations, the Bertaut approach was used to estimate the distribution of cations from XRD data. 32,33 The cation distribution was approximated using the best-matched intensity ratio, and the results are shown in Table S1. † The value of the ionic radius per molecule at the tetrahedral (rA) and octahedral (rB), theoretical lattice constant (ath), oxygen positional parameter (u), tetrahedral edge length (dAE), shared (dBE), unshared octahedral edge lengths (dBEU), and jump length of the tetrahedral (LA) and octahe (ESI). † Table S1 displays the values of all estimated structural parameters. † The fluctuations of the theoretical (ath) and actual (aexp) lattice parameters with increasing annealing temperature are identical, as shown in Table S1. Furthermore, the experimentally calculated lattice constant values from XRD data closely match the theoretical lattice constant values.

The estimated cation distribution derived from the XRD data is verified by this finding. The oxygen positioning parameter (u) has a value that is a little bit higher than the optimal value of 0.375. This has been explained by the structure's modification to account for variations in the relative effective radii of the cations in the spinel structure. With an increase in crystallite size, LA and LB were seen to have a declining tendency. The reduced behaviour as seen can be linked to both a reduced lattice parameter and a reduced gap between magnetic ions. Also, it is noted that LA > LB, which suggests that the likelihood of an electron moving between an ion at an A and B site is lower than that between a B and B site.

Bond angles directly influence the strength of magnetic exchange interactions, while interionic lengths have an opposite influence.

34 The interionic separations and bond angles of the ions in spinel ferrites are depicted in Fig. S3 (ESI). Table S2 contains the bond lengths and bond angles between the cations as determined by the relations (S14-S27) (ESI). † structural analysis Scanning electron microscopy has been used to estimate the nano-crystals' microstructure and shape accurately. The samples (Ni600, Ni800, and Ni900) are in the nanoregime, as evidenced by the SEM images of Ni0.6Zn0.4Fe1.5Al0.5O4 nanoparticles in Fig. 4a–j. For Ni1050 and Ni1200 samples, a broad size of particle is seen at higher annealing temperatures (>900 C). There was a propensity for agglomeration in all samples, which may have been caused by magnetic interactions between nanoparticles,

drying of aqueous suspensions, or electrostatic effects. This revealed the creation of spherical and evenly dispersed nanoparticles.

Co3O4 nanoparticle aggregation has been observed to exhibit a similar tendency.

35 A Lorentz distribution function can be used to explain the observed asymmetric distribution, as seen in Fig. 4k-o. According to SEM pictures, the bulk sample's average grain size was determined to be around 4 mm and the samples of Ni600, Ni800, Ni900, and Ni1050 to have average grain sizes of about 13, 20, 30, and 180 nm, respectively (Ni1200). In actuality, the temperature of annealing causes the granules to grow larger. The crystallites' coalescence at rising temperatures is what causes this increase. As seen, there is a noticeable variation between the bulk sample and Ni600 and Ni1050. These micrographs show

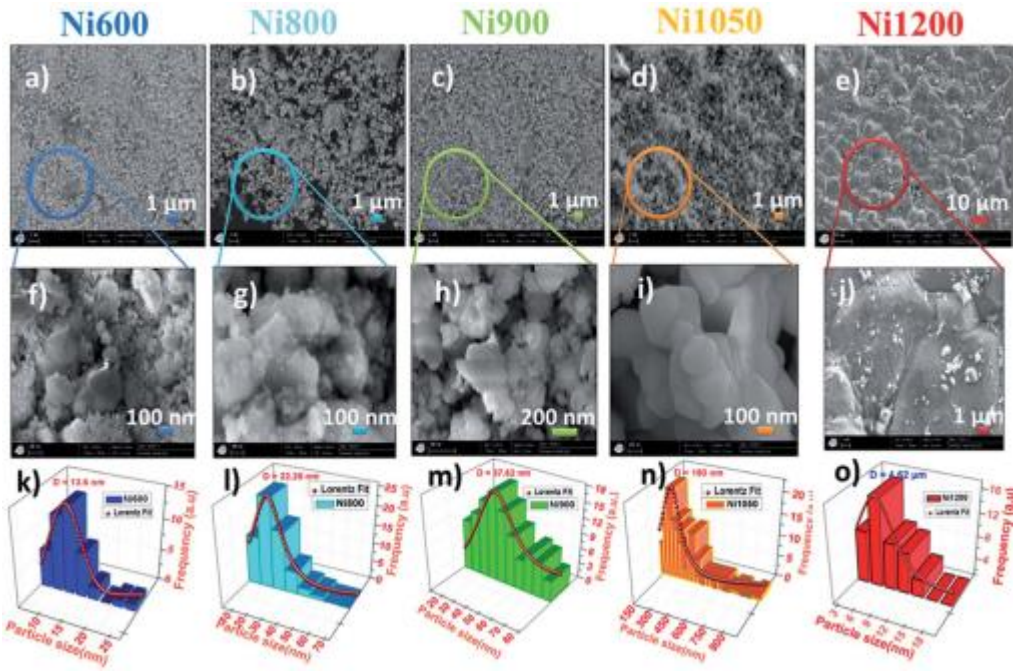

Fig. 4 SEM pictures of Ni0.6Zn0.4Al0.5Fe1.5O4 ferrite samples; (a and f) Ni600, (b and g) Ni800, (c and h) Ni900, (d and I Ni1050, (e and j) Ni1200.

The representative histograms of size distribution for of Ni0.6Zn0.4Al0.5Fe1.5O4 and their respective average size calculation by Lorentz fitting of size histograms, (k) Ni600, size is about 13.6 nm, (l) Ni800, size is about 22.2 nm, (m) Ni900, size is about 37.6 nm, (n) Ni1050, size is about 180 nm, (o) Ni1200, size is about 4 mm \sgrain boundaries and clear grains with non-uniform grain size distribution of Ni1200. The granules are almost homogeneously dispersed throughout the sample surface. This observation is congruent with the results reported by XRD analysis, detailed above. Comparing the grain size obtained by SEM with crystallite size obtained from XRD analysis, it can be concluded that each grain of sample annealed at 600, 800 and 900C almost of single crystallite nature while the grains of sample annealed at 1050 and 1200C consist of agglomeration of many crystallites. The elemental analysis of the Fe600, Fe900 and Fe1200 samples, evaluated by EDX at room temperature, are presented in Fig. S3 (ESI) (ESI). †

The spectrum con□rms the presence of all chemical elements Fe, Al, Zn, Ni and O in the synthesised Ni0.6Zn0.4- Fe1.5Al0.5O4 samples, which con□rms that there was no loss of any integrated elements and no

contamination during the process of annealing. The result of EDX predicted the needed percentage of the ingredients as well as the chemical purity of the samples, denoting a homogeneous chemical composition. Raman analysis Additional structural and complimentary features can be gained by the examination of the Raman spectra. Confocal Raman spectroscopy has been widely employed as an excellent tool to research the cation disorder, the lattice dynamics and structural transition in ferrites due of their sensitivity and their high spatial resolution to explore atomic vibrations. In order to verify the chemical impurity and to con□rm the formation of our simples, Raman spectra at room temperature in the region of 120 cm1 to 850 cm1 by using 540 nm laser excitation of Ni0.6Zn0.4- Fe1.5Al0.5O4 nanoparticles and bulk synthesised by annealing at 600, 800, 900, 1050 and 1200 C are presented in Fig. 5a. The factor group analysis predicts the following modes in spinel:36

$$\zeta = A_{1g}(R) + E_g(R) + T_{1g} + 3T_{2g} + 2A_{2u} + 2E_u + 4T_{1u}(IR) + 2T_{2u}$$

where, (IR) and (R) indicate infrared active vibrational and Raman modes, respectively. For spinel ferrite, it is well known that the group theory predicts that Raman active modes (A1g + Eg + 3T2g) are observed at ambient conditions and they are associated to the motion of O ions and both the A-site and B-site ions and four infrared active modes (4T1u) for the Fd3m space group. 14 The A1g Raman mode is associated to the symmetric stretching of the oxygen atom with respect to metal ion in tetrahedral sites. The Raman mode corresponds to the symmetric bending of the oxygen atom with respect to the metal ion at the octahedral site and the T2g(3) and T2g(2) Raman modes are due to the symmetric and asymmetric bending of

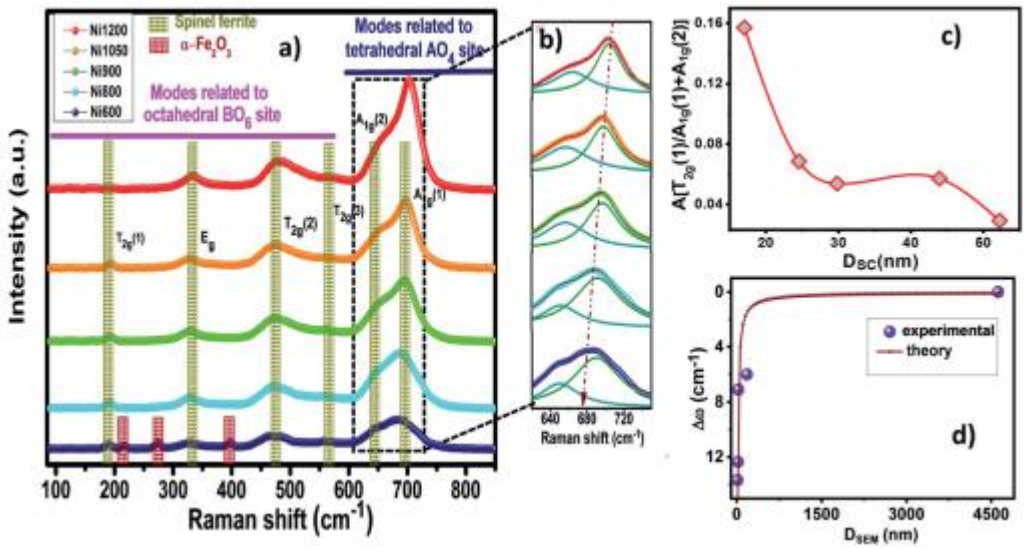

Fig. 5 (a) The Raman spectra of Ni0.6Zn0.4Al0.5Fe1.5O4 NPs at different annealing temperature with assigned symmetry types of the Raman active bands, recorded in the region of 100–850 cm1 at 300 K. (b) An enlarged view of the A1g modes. (c) The crystallite size Dsc dependence of the area ratio between the bands associated with the octahedral and tetrahedral sites. (d)

The relative Raman shifts Du of the A1g mode vs. particle size DSEM, line is the fitted result obtained by the confinement model oxygen atom in M–O band at octahedral site. Finally, the T2g(1) phonon corresponds to the translation movement of the whole MO4 tetrahedral units. 37 So accordingly, all the Raman active bands of

NZFAO samples are assigned to the theoretical vibrational mode of Fd3m space group and illustrated in Table S3 (ESI) (ESI). †

The observed Raman modes are in good agreement with the literature reports.

38 In the Ni600 nanoparticle sample, the peaks centred on 216, 274 and 397 cm1 could be attributed to A1g, Eg(1) and Eg(2) vibrational modes of hematite a-Fe2O3, 39 respectively, which is consistent with the results of the XRD. No additional peak corresponding to any other iron oxide phase is present for the other compounds, thus confirming the monophasic composition throughout. In order to determine lattice effect, the natural frequency, and the positions of the peak and its full width at half maximum (FWHM), Lorentzian line shape was used to t the Raman spectra (Fig. S4, (ESI)†). In spinel ferrites, the modes above 600 cm1 are belonged to the vibrations of the oxygen atoms in tetrahedral sites AO4 groups, whereas the modes below this frequency are related to the motion of the oxygen atoms in octahedral sublattice (Omodes) (Omodes). 40 Additional shoulder mode are probably related to a breakdown of the momentum conservation rule since the particle diameter are innocently smaller than the wavelength of the exciting radiation.

Focusing on the most intense A1g mode, a clear increase in intensity and blue shi along with the line broadening behaviour can be seen with an increase of annealing temperature. The ratio of these signals is directly correlated to the degree of inversion of the spinel. 42 As in spinel ferrite, the distribution of trivalent and divalent cations can change due to migration of metal ions from octahedral (B) to tetrahedral (A) sites and vice versa.

CONCLUSION

MgNi ferrites are soft magnetic material and very important from technological point of view. The unique properties of MgNi ferrite nanoparticles such as low coercivity, low magnetic losses, high resistivity (106 Ω-cm), moderate saturation magnetization, good mechanical hardness, chemical stability over wide range of temperature, high magnetic permeability and superparamagnetic in nature makes it promising candidates for electrical, electronic and bio-medical applications. In this work we have enhanced the magnetic properties of MgNi ferrite system in terms of substituting Mg2+ ions, synthesis methods and annealing temperature. Mg2+ ions have been used to replace the Ni2+ ions. As Mg2+ ion are nonmagnetic the net magnetic moment of the lattice decreases with increase in Mg2+ ion composition consequently decreases the coercivity, saturation magnetization and retentivity of the synthesised material. In order to synthesise the MgNi ferrite particles in the nano range, sol-gel method has been used because this method has control over the size of synthesised particles. In order to visualise the effect of annealing temperature, the synthesised material is annealed at two temperatures i.e., 900◦C and 1100◦C.The structural, morphological, magnetic and elastic properties of all the prepared samples have been analysed using XRD, FESEM, EDX, FTIR, Raman, UV-Vis and VSM respectively. The variation in structural, morphological and magnetic properties have been explained in terms of variation of Mg2+ ion composition, distribution of cations in different sub-lattices, synthesis methods and annealing temperatures. In first objective, all the samples have been processed by sol-gel method annealed at 900◦C temperature. The variations in structural, morphological and magnetic properties have been explained in terms of Mg2+ ion

REFRENCES

1 R. Valenzuela, "Novel applications of ferrites," Physics Research International, 2012. [Online]. Available: https://doi.org/10.1155/2012/591839

2 J. Haspers, "Ferrites-their properties and applications," in Modern Materials. Elsevier, 1962, vol. 3, pp. 259–341. [Online]. Available: https://doi.org/10.1016/ B978-1-4831-9657-2.50009-7

3 M. Pardavi-Horvath, "Microwave applications of soft ferrites," Journal of Magnetism and Magnetic Materials, vol. 215, pp. 171–183, 2000. [Online]. Available: https://doi.org/10.1016/s0304-8853(00)00106-2

4 J. Wei, K. Niikura, T. Higuchi, T. Kimura, H. Mitomo, H. Jinnai, Y. Joti, Y. Bessho, Y. Nishino, Y. Matsuo et al., "Yolk/shell assembly of gold nanoparticles by size segregation in solution," Journal of the American Chemical Society, vol. 138, no. 10, pp. 3274–3277, 2016.

5 H. Schafer, K. Kupper, and J. Wollschlager, "Oxidized mild steel an efficient anode for electrocatalytically initiated water splitting," ChemSusChem, vol. 8, pp. 3099– 3110, 2015.

6 G. F. Dionne, D. E. Oates, D. H. Temme, and J. A. Weiss, "Ferrite-superconductor devices for advanced microwave applications," IEEE Transactions on Microwave theory and Techniques, vol. 44, pp. 1361–1368, 1996.

A. Verma, M. Alam, R. Chatterjee, T. Goel, and R. Mendiratta, "Development of a new soft ferrite core for power applications," Journal of Magnetism and Magnetic Materials, vol. 300, pp. 500–505, 2006. [Online]. Available: https://doi.org/10.1016/j.jmmm.2005.05.040

7 G. Stojanovic, M. Damnjanovic, V. Desnica, L. Zivanov, R. Raghavendra, P. Bellew, and N. Mcloughlin, "High-performance zig-zag and meander inductors embedded in ferrite material," Journal of Magnetism and Magnetic Materials, vol. 297, pp. 76–83, 2006. [Online]. Available: https://doi.org/10.1016/j.jmmm.2005.02.058

8 G. I. Likhtenshtein, J. Yamauchi, S. i. Nakatsuji, A. Smirnov, and R. Tamura, Nitroxides. Springer, 2012. [Online]. Available: https: //doi.org/10.1007/978-3-030-34822-9

9 T. Thomson, L. Abelmann, and H. Groenland, "Magnetic data storage-past present and future." Springer, 2008, pp. 237–306.

10 M. E. F. Brollo, R. López-Ruiz, D. Muraca, S. J. Figueroa, K. R. Pirota, and M. Knobel, "Compact ag@ fe3o4 core-shell nanoparticles by means of single-step thermal decomposition reaction," Scientific reports, vol. 4, no. 1, pp. 1–6, 2014.

11 R. Popovtzer, A. Agrawal, N. A. Kotov, A. Popovtzer, J. Balter, T. E. Carey, and R. Kopelman, "Targeted gold nanoparticles enable molecular ct imaging of cancer," Nano letters, vol. 8, no. 12, pp. 4593–4596, 2008.